Acta Oceanol. Sin., 2019, Vol. 38, No. 5, P. 51–61
https://doi.org/10.1007/s13131-018-1339-5
http://www.hyxb.org.cn
E-mail: hyxbe@263.net

Spatial and temporal evolution of landfast ice near Zhongshan Station, East Antarctica, over an annual cycle in 2011/2012

Jiechen Zhao[1, 2, 3], Qinghua Yang[4, 5*], Bin Cheng[6], Matti Leppäranta[7], Fengming Hui[8*], Surui Xie[9], Meng Chen[10], Yining Yu[8], Zhongxiang Tian[2], Ming Li[2], Lin Zhang[2]

[1] College of Oceanic and Atmospheric Sciences, Ocean University of China, Qingdao 266100, China

[2] National Marine Environmental Forecasting Center, Beijing 100081, China

[3] First Institute of Oceanography, Ministry of Natural Resources, Qingdao 266061, China

[4] Guangdong Province Key Laboratory for Climate Change and Natural Disaster Studies, School of Atmospheric Sciences, Sun Yat-sen University, Zhuhai 519082, China

[5] Southern Marine Science and Engineering Guangdong Laboratory (Zhuhai), Zhuhai 519082, China

[6] Finnish Meteorological Institute, Helsinki 00101, Finland

[7] Institute of Atmospheric and Earth Sciences, University of Helsinki, Helsinki 00014, Finland

[8] College of Global Change and Earth System Sciences (GCESS), Beijing Normal University, Beijing 100875, China

[9] School of Geosciences, University of South Florida, Tampa 33620, USA

[10] Meteorological Service of Youyang Tujia and Miao Autonomous County, Chongqing 409800, China

Received 9 January 2018; accepted 26 March 2018

Abstract

Annual observations of first-year ice (FYI) and second-year ice (SYI) near Zhongshan Station, East Antarctica, were conducted for the first time from December 2011 to December 2012. Melt ponds appeared from early December 2011. Landfast ice partly broke in late January, 2012 after a strong cyclone. Open water was refrozen to form new ice cover in mid-February, and then FYI and SYI co-existed in March with a growth rate of 0.8 cm/d for FYI and a melting rate of 2.7 cm/d for SYI. This difference was due to the oceanic heat flux and the thickness of ice, with weaker heat flux through thicker ice. From May onward, FYI and SYI showed a similar growth by 0.5 cm/d. Their maximum thickness reached 160.5 cm and 167.0 cm, respectively, in late October. Drillings showed variations of FYI thickness to be generally less than 1.0 cm, but variations were up to 33.0 cm for SYI in March, suggesting that the SYI bottom was particularly uneven. Snow distribution was strongly affected by wind and surface roughness, leading to large thickness differences in the different sites. Snow and ice thickness in Nella Fjord had a similar "east thicker, west thinner" spatial distribution. Easterly prevailing wind and local topography led to this snow pattern. Superimposed ice induced by snow cover melting in summer thickened multi-year ice, causing it to be thicker than the snow-free SYI. The estimated monthly oceanic heat flux was ~30.0 W/m^2 in March–May, reducing to ~10.0 W/m^2 during July–October, and increasing to ~15.0 W/m^2 in November. The seasonal change and mean value of 15.6 W/m^2 was similar to the findings of previous research. The results can be used to further our understanding of landfast ice for climate change study and Chinese Antarctic Expedition services.

Key words: landfast ice, thickness, oceanic heat flux, Prydz Bay, East Antarctica

Citation: Zhao Jiechen, Yang Qinghua, Cheng Bin, Leppäranta Matti, Hui Fengming, Xie Surui, Chen Meng, Yu Yining, Tian Zhongxiang, Li Ming, Zhang Lin. 2019. Spatial and temporal evolution of landfast ice near Zhongshan Station, East Antarctica, over an annual cycle in 2011/2012. Acta Oceanologica Sinica, 38(5): 51–61, doi: 10.1007/s13131-018-1339-5

1 Introduction

In contrast to the rapid decline of sea ice extent and volume in the Arctic, the total Antarctic sea ice area has increased by about 0.4×10^6 km^2 since the late 1970s (Liu et al., 2010; Parkinson and Cavalieri, 2012). Sea ice observations from space-borne sensors and *in situ* surveys have played a major role in understanding the variability of Antarctic sea ice. Ice thickness is a key sea ice property, however, remote sensing of large-scale sea ice thickness from space remains a major challenge (Kwok and Sulsky, 2010; Worby et al., 2008; Lu et al., 2014). Field observations are the traditional approach to map Antarctic landfast ice thickness.

Landfast ice forms along the Antarctic coastline and shelf edges, typically in narrow bands with a varying width up to 150 km from the continent (IPCC, 2013). It generally comprises between 5% (winter) and 35% (summer) of the Antarctic sea ice area (Fraser et al., 2012), and a greater fraction of ice volume in East Antarctica (Giles et al., 2008); therefore, landfast ice is an import-

Foundation item: The National Natural Science Foundation of China under contract Nos 41876212, 41406218 and 41676176; the Polar Strategy Project from Chinese Arctic and Antarctic Administration under contract No. 20120317; the Opening Fund of Key Laboratory of Land Surface Process and Climate Change in Cold and Arid Regions, CAS, under contract Nos LPCC2018001 and LPCC2018005.
*Corresponding author, E-mail: yangqh25@mail.sysu.edu.cn; huifm@bnu.edu.cn

ant factor in understanding Antarctic sea ice cover changes. Furthermore, near-shore landfast ice can be feasibly used to examine the variations of Antarctic sea ice thickness with repeat access for sea ice measurements (Heil et al., 2011).

The Antarctic Fast-Ice Network (AFIN) has been established to coordinate landfast ice observations from scientific stations operated by international contributors (Heil et al., 2011). Research focusing on landfast sea ice in Lützow-Holm Bay found that deep snow cover on multi-year ice (MYI) led to large thickness growth during summer due to snow-ice formation at the top of the ice, but only minor growth during winter (Kawamura et al., 1997). Gough et al. (2013) investigated evolution of multi-year snow-ice in McMurdo Sound and found that ice temperature remaining around –2.5°C until the first week of March, and ~200 cm thick ice showed bottom melting at a constant rate of 0.2 cm/d from mid-March to the end of April. In the Atka Bay, landfast ice observations suggested that super-cooled water including platelet ice contributes strongly to sea-ice formation, snow cover was very heterogeneous throughout the entire bay and strong easterly winds lead to thicker sea ice and snow cover in the west (Hoppmann et al., 2012). Long-term field observations in the Davis Station, Prydz Bay, showed that the maximum ice thickness had inter-annual variation with a decadal increase from 130 cm to 180 cm (Heil et al, 1996, 2006).

At the Zhongshan Station (ZS), field work conducted in winter 1992 focused on first-year ice (FYI) and found that it was mainly composed of congelation ice (He et al., 1998). Investigation of landfast ice in Nella Fjord in summer 2003 showed that snow and ice thickness both increased along the prevailing wind direction, and average ice thickness was 170.0 cm, which may be a sign of MYI (Tang et al, 2006). Annual mass balance and heat flux were observed and estimated from mid-February to late November of 2006, providing important material comparison with the current study, but MYI observations were not included at this time (Lei et al., 2010).

In this paper, spatial and temporal evolution of landfast ice near ZS was analyzed based on the field observations from December 2011 to December 2012. Landfast ice breakup and refreezing were virtually recorded from the shore. Second-year ice (SYI) observations were carried out for the first time, accompanied by FYI observations near ZS. Snow thickness was recorded by a sonar and stainless-steel ruler, while ice thickness was observed manually by borehole measurements from March to December. The winter spatial distribution of snow and ice thickness inside Nella Fjord was assessed for the first time. The oceanic heat flux was estimated by the residual method. Through analysis of these observations, the primary conditions of the annual FYI and SYI cycle, were provided for scientific goals and expedition services.

2 Observations and methods

2.1 *Meteorology*

The ZS (69°22′S, 76°22′W) is located in the Larseman Hill of East Antarctica, close to the Australian Davis Station and Russian Progress Station (Fig. 1). All these stations are operated year-

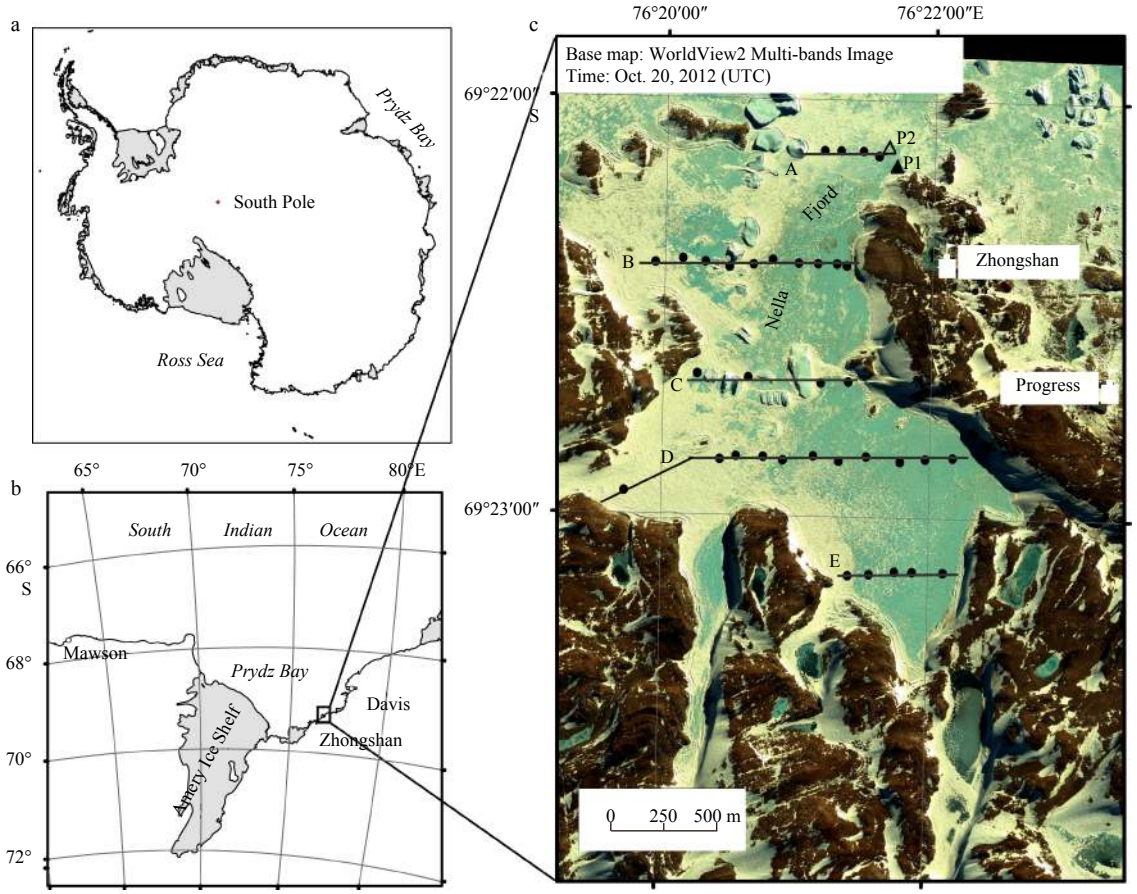

Fig. 1. Location of the Prydz Bay (a) and Zhongshan Station (b); observation field in the Nella Fjord: fixed Sites P1 (solid triangle) and P2 (open triangle), and Sections A, B, C, D and E with measurement sites (black dots) (c).

round. In the operational year 2011/2012, annual observations at ZS started in December 2011 after R/V *Xuelong*, Chinese polar icebreaker, arrived with observation devices and continued until December 2012 when snow and ice melted heavily.

Meteorological parameters including surface pressure, air temperature, wind speed and direction, and humidity were measured by the ZS automatic weather station (WMO No. 89573) at an elevation of 15 m (Fig. 2a). Cloudiness and visibility were recorded manually by a meteorologist at UTC 00:00, 06:00, 12:00 and 18:00 every day. Air temperature on the ice was recorded every minute by a sensor T109 (Campbell Scientific, Inc., Logan, UT, USA) deployed on a tripod (Figs 2b and c) near the ice observation Site P1 (Fig. 1c) from March 25 to November 30, 2012. The altitude of the sensor T109 was 2 m.

2.2 *Snow and ice*

2.2.1 *Fixed sites observations*

The evolution of landfast ice, including breakage and refreezing, was monitored manually in the sound of Nella Fjord by a digital camera mounted on the shore. Photographs were taken every 5 d from December 2011 to March 2012. The photographs covered the area of Sites P1 and P2 (Fig. 1c). Part of the nearshore landfast ice could survive to next winter and become SYI. Those photographs offered a good material to detect the boundary between FYI and SYI (Fig. 2b).

Manual snow and ice thickness measurements were carried out at P1 and P2, about 100 m and 200 m off the shore, respectively (Fig. 1c). The measurements started from March 10, 2012 and the frequency was 2–5 d, but paused during the two months of polar night (end of May to end of July) and recovered after then. Snow thickness was measured by a stainless-steel ruler, which was pushed into the snow down to the ice surface to obtain the thickness (Fig. 2d). The accuracy was 0.1 cm. Ice thickness was measured by a gage with the accuracy of 0.1 cm in boreholes drilled by a Kovacs ice auger (5 cm in diameter) (Figs 2e and f). At every observation, boreholes were drilled carefully to avoid repeating the previous ones. Usually one borehole was drilled at P1 for each observation day, but occasionally three boreholes were drilled to assess the variations of thickness from different boreholes. However, more than three boreholes were drilled for every observation day at P2, because considerable large variations in ice thickness among different boreholes were found there in the initial measurements.

A tripod was deployed near P1 (Fig. 2b) and a sonar sensor SR50A (Campbell Scientific, Inc., Logan, UT, USA) was mounted to it to automatically record the snow thickness (Fig. 2c). An infrared sensor SI-111 (Campbell Scientific, Inc., Logan, UT, USA) was also mounted to it to record the snow/ice surface temperature. The sampling frequency of both sensors was 1 min, and the observation period was from March 25 to November 30, 2012.

2.2.2 *Section observations*

Five sections were positioned to survey snow and ice thickness inside the Nella Fjord from September 29 to October 2, 2012. This was the first time that winter spatial observations had been carried out in this area, including 34 measurement sites along five sections (Fig. 1c). The snow and ice thickness measurements were made manually and in the same way as for the fixed sites. The location of each site was recorded with a handheld GPS receiver. Spatial distributions in the whole fjord were obtained using a Kriging interpolation method.

3 Results

3.1 *Meteorological conditions*

In the annual cycle of December 2011 to December 2012, the mean air temperature was –10.4°C (Fig. 3b). The highest monthly mean air temperature occurred in January 2012 (–0.6°C) and the lowest was in July 2012 (–19.6°C). The warmest and coldest daily mean air temperatures were 6.1°C and –34.5°C, observed on January 18 and May 24, respectively. The mean relative humidity was 54% (Fig. 3c). The mean wind speed was 7.1 m/s, and the highest hourly mean wind speed was 32.8 m/s recorded on June 29 (Fig. 3e). Precipitation was not observed at ZS, but it was available from Progress Station. Large accumulated precipitation oc-

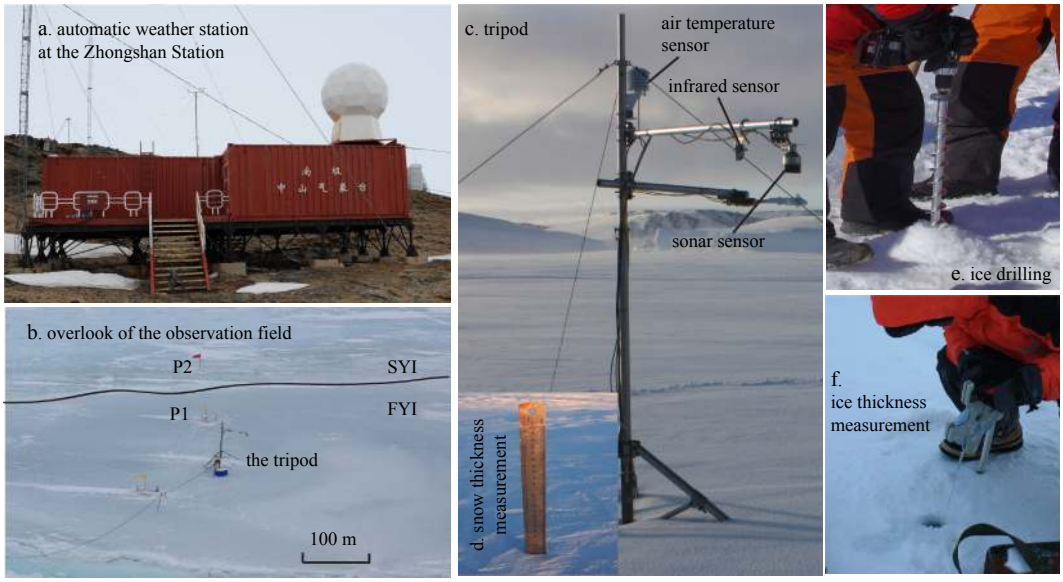

Fig. 2. Automatic weather station at Zhongshan Station (a); overlook of the observation field, the black line represents the boundary of FYI and SYI (b); photograph of the tripod (c); the stainless-steel ruler for snow thickness measurement (d); ice drilling by a Kovacs ice auger (e); and ice thickness measurement by a gage (f).

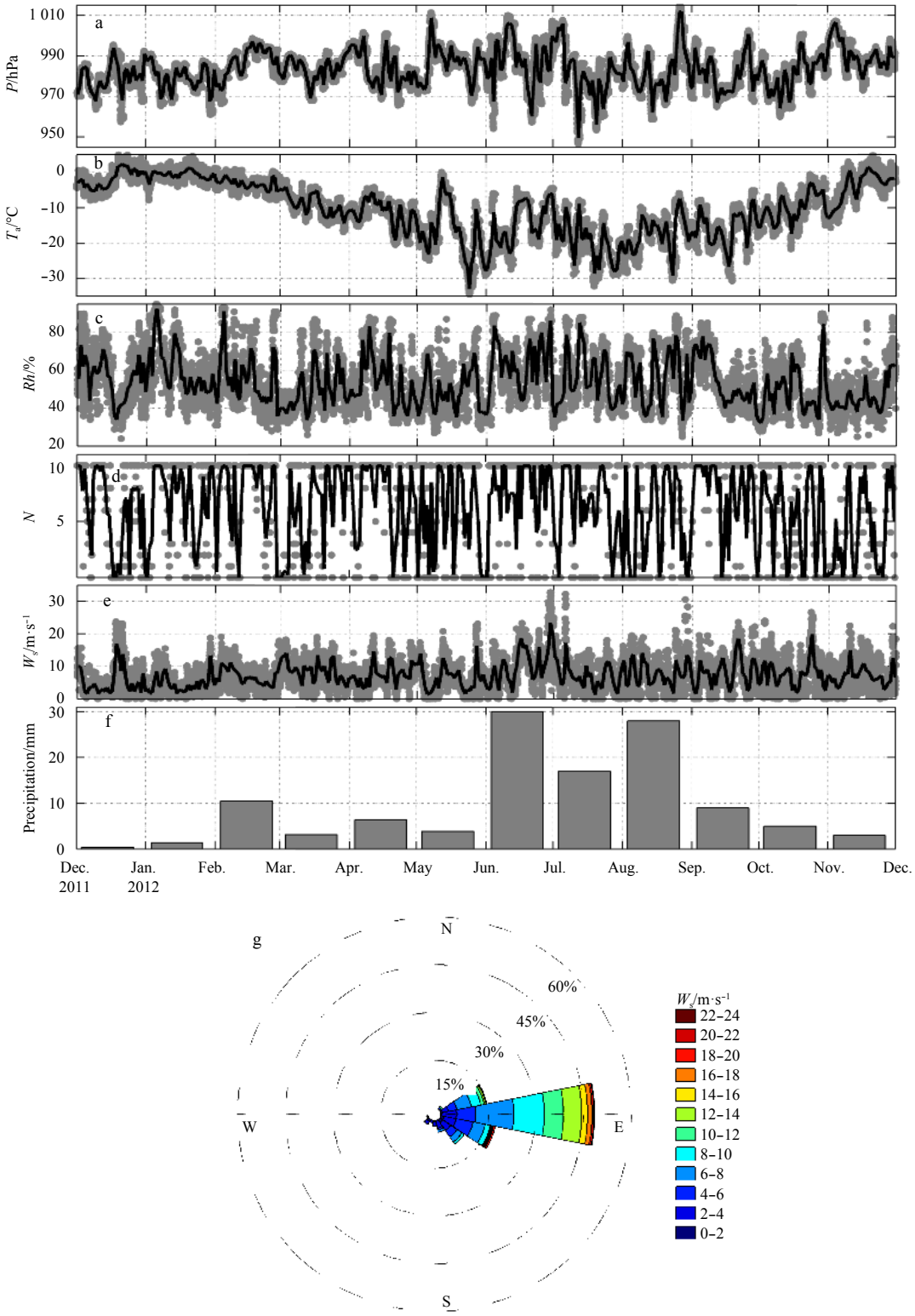

Fig. 3. The time series of surface air pressure (a), surface air temperature (b), surface relative humidity of air (c), cloudiness (d), surface wind speed (e), precipitation (f), and wind rose diagram (g). Gray dots represent hourly data in a, b, c and e, but 6-hourly data in d. Black lines represent the daily mean values. The gray bar in f is the monthly accumulated precipitation at Progress Station.

curred during June-August was 18–30 mm per month, while other months were less than 10 mm per month (Fig. 3f). The prevailing wind came from the east, accounting for 48% of the annual cycle period (Fig. 3g). Snowfall induced by the Prydz Bay cyclones in Larseman Hill was frequent and snow was blown away by the strong winds, which redistributed the snow spatial pattern. Therefore, the measured snow accumulation was not sufficiently accurate to represent the real snowfall amount.

Compared with the climatology from Year 1989 to 2014, the annual mean air temperature was 0.6°C lower, relative humidity was 4% lower, and wind speed was 0.1 m/s larger.

3.2 *Ice breakup and refreezing*

The landfast ice characteristics shown in Fig. 4 were charted by photographs taken along the coast, field records, and high-resolution satellite images. Ice floes of different sizes transported by strong prevailing easterly winds were accumulated in the northeast of ZS and usually survived over the summer to become MYI (Area I in Fig. 4a). The landfast ice at the sound of Nella Fjord started to melt at the end of October and melt ponds were apparent from early December, 2011 (Fig. 4b). Ice was partly broken up from January 23, 2012 after one strong cyclone visit (Area II in Fig. 4a). Then, open water was present for about 20 d, until mid-February, when the day-night melting-freezing cycles commenced. Ice was formed again at the end of February to start a new FYI. Melt ponds were common over Area III, but surrounding islands and small icebergs kept the ice unbroken. Area IV was covered by thick snow and melting was common in the snow surface, but the ice beneath the snow survived to the next winter. Therefore, ice in Areas III and IV was MYI. According to field records, ice at P2 was SYI, which had different evolution compared with MYI inside the fjord.

The ice breakup and refreezing time in late January and mid-February were similar to observations near ZS in 2006 (Lei et al., 2010) and at Davis Station since 2000 (Heil et al., 2006). The breakup date and extent of breakage are strongly dependent on the cyclone strengths and timing. The landfast ice could survive to the next winter, indicating that ice in the Nella Fjord does not disappear by melting, but by dynamic processes (Yang et al., 2015a). The same phenomena was also observed on the Arctic Siberian coast (Yang et al., 2015b).

3.3 *Snow thickness*

Snow thickness observed automatically at the sonar site and manually at P1, P2, and the tripod are illustrated in Fig. 5. There was a close relationship between the automatic and manual observations at the tripod site, with Pearson's correlation coefficient of 0.71. This implies that the sonar sensor could record the changes of snow thickness with high reliability. Between July and August all measurement sites showed large snow accumulation, but the values were considerably different. Considering the close locations, this phenomenon suggested that snow accumulation was strongly affected by the ice surface roughness and had large spatial variations. Snowfall near ZS was caused by the moisture transport induced by strong cyclones, and strong wind coming along usually redistributed the snow cover quickly. Five major snowfall events occurred and were recorded by the sonar after June. Half of the accumulated snow was blown away by a strong wind within 24 h after the snowfall events S1 and S2. In S5, snow thickness reduced from 31.0 cm to 15.0 cm in 72 h because of the strong wind.

Before June, ice surface was almost snow-free. The maximum thickness record by ruler at the tripod site was 26.0 cm on October 29, but 31.0 cm measured by sonar on October 31 during the snowfall event S5. Manual observations missed this important largest value and date, but sonar captured it.

3.4 *Ice thickness*

The evolution of FYI at P1 and SYI at P2 is illustrated in Fig. 6. The first field measurement was carried out on March 10 at P2 and the ice thickness was 116.0 cm. The first measurement at P1 was conducted one day later on March 11 and the ice thickness was 22.0 cm, about 100 cm less than SYI at P2 (Fig. 6a). The FYI grew continuously from March to October. From March to May, the mean growth rate was 0.7 cm/d (Fig. 7), and between August and October ice growth slowed down to the mean rate of 0.4 cm/d. The maximum growth rates were around 1.0 cm/d, similar to the observations of the landfast ice off ZS in 2006 (Lei et al., 2010). The maximum thickness of FYI was 160.5 cm observed on Octo-

Fig. 4. Landfast ice characteristics in the Nella Fjord during January 2012 (a) and ice evolution in the sound of the Nella Fjord (b). In Fig. 4a, the white circle represents the location of the camera and the black triangle shows the area of the coverage of the photographs.

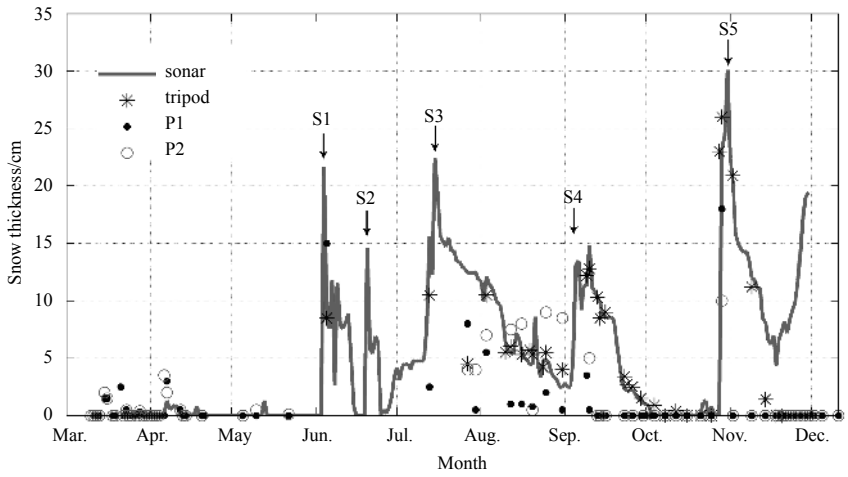

Fig. 5. Observed snow thickness at P1, P2, the tripod, and by the sonar sensor. Five major snowfall events are marked by S1, S2, S3, S4 and S5.

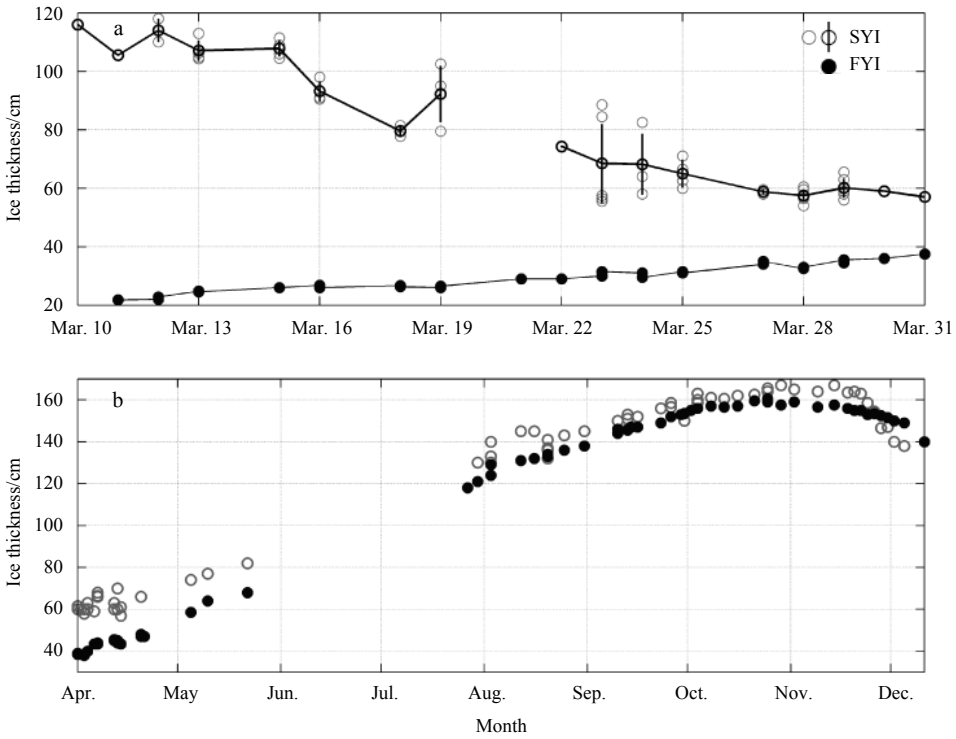

Fig. 6. Ice thickness of FYI and SYI in March (a) and April–December 2012 (b). Grey circles represent each drilling result, black circles represent averaged values and bars are standard deviation. Black dots represent each drilling result for FYI.

ber 25, 2012. This was less than 174.0 cm in 2006 (Lei et al., 2010), 176.0 cm in 2010, and 186.0 cm in 2011 observed by ZS wintering personnel. Bottom melting started from the end of October, with a rate of 0.4 cm/d. Melting became a little weaker in November, 0.3 cm/d, and in December it increased to 1.0 cm/d. During the no-data period in the polar night, mean growth rate was estimated as 0.8 cm/d.

The SYI showed a quite different curve in March, 2012, melting with a monthly mean rate of 2.7 cm/d (Fig. 6a), leading to ice thickness reduction from 116.0 cm (March 10) to 57.0 cm (March 31). On March 10 and 11, an easy-drill-through layer was observed at 60.0–80.0 cm depth below the ice surface. In the first two weeks of April, SYI thickness changed slightly with a stable value of about 60.0 cm. From April 15, SYI began to grow quickly. The growing trend was similar to FYI, but SYI was generally 10.0 cm–20.0 cm thicker than FYI. SYI growth slowed down in August and began melting at the end of October. The maximum thickness of SYI was 167.0 cm on October 29. Monthly mean melting rate in November was 0.6 cm/d, twice that of FYI, but in December it was only 0.5 cm/d, half of the FYI melt rate. The larger value of SYI in Fig. 7 during November and December suggested that SYI began to show larger spatial variation during the melting season.

The FYI growth and simultaneous SYI ablation in March have previously been studied in detail and SYI ablation was attributed to nonlinear temperature profile and internal melting (Zhao et al., 2017).

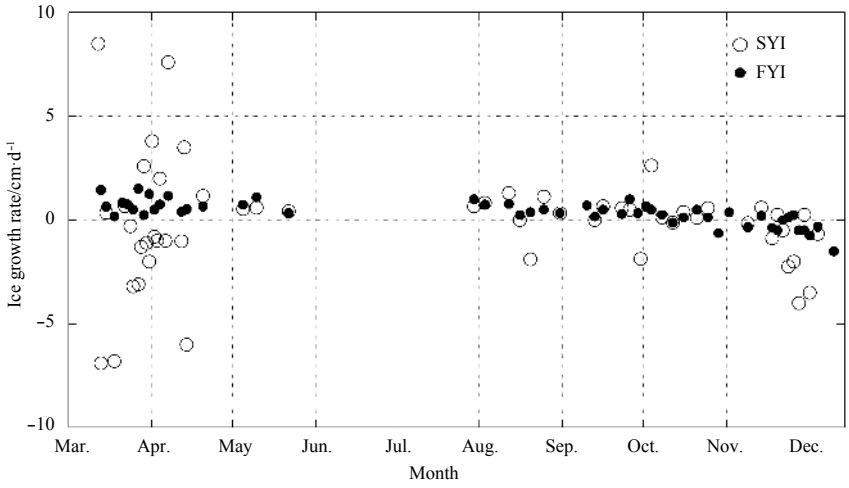

Fig. 7. Ice growth rate of FYI and SYI from March to December 2012.

3.5 *Observations variation*

At P1, ice thickness variations between different boreholes for each observation day were smaller than 1.0 cm. Considering the flat surface, this indicated that the FYI grew synchronously and the bottom was fairly smooth.

The ice thickness variation at P2 is shown in Table 1. A total of 17 visits were made to P2 in March, and in each visit, at least three drillings were performed. On March 23, six boreholes were drilled, the maximum number in this month. The measured ice thickness varied from 55.5 cm to 88.5 cm, leading to the largest thickness difference among the borehole sets (33.0 cm). The mean ice thickness was 81.4 cm in March. The data presented in Table 1 suggest that SYI thickness had a large spatial deviation in a small spatial scale (~10 m) and the largest variation reduced over time, likely because thinner ice grows more rapidly. The recorded ice surface unevenness was around 5.0–10.0 cm during the winter, which implies that 30% of the variations came from an uneven surface and 70% came from an uneven bottom.

Table 1. Statistics of SYI thickness variation at P2 in the different months

	Mar.	Apr.	Aug.	Sep.	Oct.
Number of measurements	17	10	6	7	7
Max drillings in single measurement	6	4	5	3	3
Mean ice thickness/cm	81.4	61.8	141.5	153.0	162.6
Largest variation/cm	33.0	10.0	10.0	7.0	4.5

3.6 *Regional distribution*

The spatial mean snow thickness was 11.3 cm inside the Nella Fjord. Snow cover was thin in the eastern part and thick in the western part of the fjord. The thickest snow was recorded in the eastern end of Section D, exceeding the range of the 100-cm ruler. Small icebergs influenced the snow distribution, and snow around them was 5.0 cm–10.0 cm thicker than in other areas (Fig. 8a). The overall distribution of snow in this fjord was determined by the surface wind direction and topography. The prevailing strong easterly winds blew the snow westward, and the north-south oriented hills in the eastern side blocked the snow drift, forcing the snow to accumulate there, leading to a "west thicker, east thinner" pattern, as shown in Fig. 8b.

Similar to the snow thickness distribution, the ice thickness in the east was generally larger than in the west, and the spatial correlation coefficient between snow and ice thickness was 0.52. Ice in 55% of the 34 sites was thicker than 200.0 cm, and the maximum ice thickness was 307.0 cm in Section D. The spatial mean ice thickness was 202.7 cm. A similar "west thicker, east thinner" pattern and maximum ice thickness of 201.0 cm was observed in January 2003 in the Nella Fjord (Tang et al., 2007).

3.7 *Oceanic heat flux estimations*

In the classic Stefan's Law, ice surface temperature is used to estimate ice thickness in the growth season. This law has been used inversely for oceanic heat flux estimation; however, ice surface temperature is rarely available, and therefore it is usually replaced by surface air temperature. In this study, we were able to obtain snow/ice surface temperature (T_o), field surface air temperature (T_a), and surface air temperature at ZS (T_{zs}) at the same time. The daily mean values in Fig. 9 show that T_o was (1.3 ± 1.5)°C lower than T_a. The cases $T_o < T_a$ accounted for 83% throughout the time series. T_a was (0.1 ± 3.4)°C larger than T_{zs}. The difference between T_a and T_{zs} was generally oscillating within a range of ±5.0°C.

The residual method (Mcphee and Untersteiner, 1982) was used to estimate the oceanic heat flux for FYI at P1 with the three differently measured temperatures described above. This method has been already widely used in previous studies (Perovich and Elder, 2002; Lytle et al., 2000; Purdie et al., 2006; Lei et al., 2010). The residual method was also used with a full numerical model of ice thickness by Yang et al. (2015a).

At the base of the sea ice, assuming a quasi-steady heat flux, the thermal energy balance is simplified by

$$\rho_i L_f \mathrm{d}H/\mathrm{d}t = k_i (T_f - T_o)/H - F_w, \quad (1)$$

where ρ_i is the sea ice density at the basal layer, L_f is the sea ice latent heat of freezing, $\mathrm{d}H/\mathrm{d}t$ is the ice growth rate, k_i is the thermal conductivity of sea ice, T_f is the sea water freezing point, T_o is the ice surface temperature, H is the ice thickness, and F_w is the oceanic heat flux.

In Eq. (1) the term on the left-hand side represents latent heat flux (F_l), resulting from ice growth, and the first term on the right-hand side represents the conductive heat flux (F_c) at the base ($F_c \geqslant 0$). For simplification, the thermal inertia is ignored in the

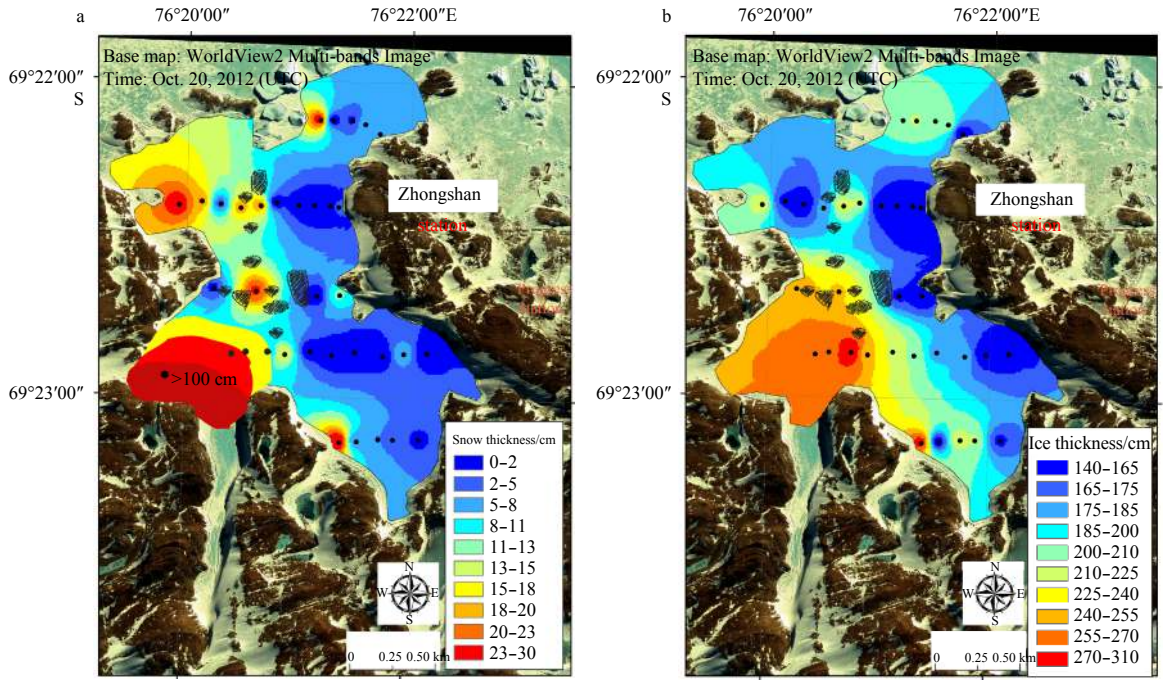

Fig. 8. Snow (a) and ice (b) thickness spatial distribution in the Nella Fjord measured from September 29 to October 2, 2012. The black solid circles represent measurement sites. The black slashes represent the locations and shape of small icebergs.

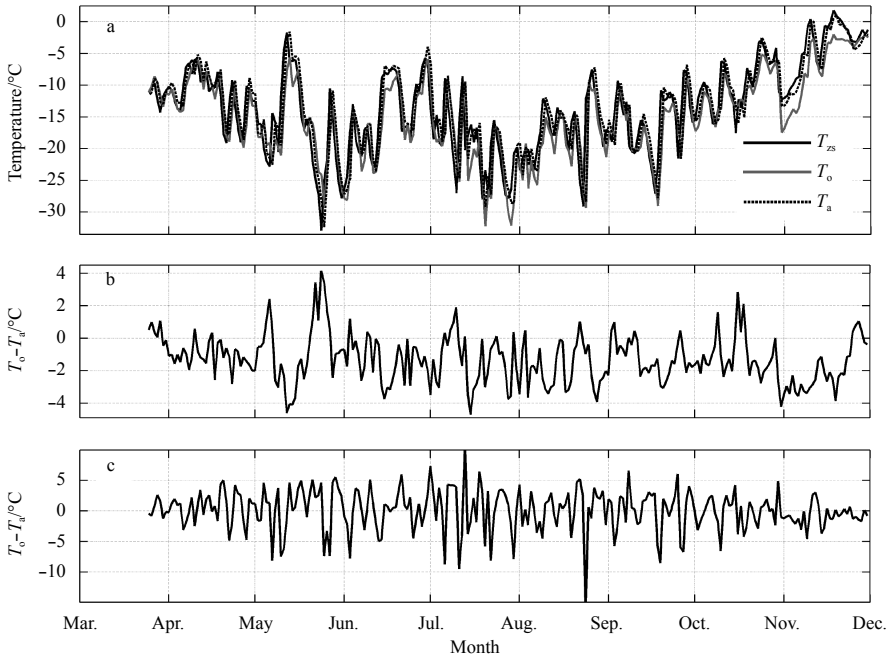

Fig. 9. Time series of daily mean snow/ice surface temperature (T_o), field air temperature (T_a) and surface air temperature at ZS (T_{zs}) (a), $T_o - T_a$ (b) and $T_a - T_{zs}$ (c).

quasi-steady approach.

In the calculations, a three-record moving average was applied to the original observations, and then the observed ice thickness was linearly interpolated into daily values. The growth rate was calculated based on the interpolated daily values. Ice density was set to 910 kg/m^3, sea ice latent heat of freezing was set to 333.4 kJ/kg, and thermal conductivity was set to 2.2 W/(m·°C). To examine the sensitivities of F_c to the temperature from different sources, T_o, T_a and T_{zs} were used separately. F_c calculated with T_o was (2.7 ± 3.9) W/m^2 larger than that with T_a, and (2.2 ± 9.1) W/m^2 larger than that with T_{zs}.

The heat fluxes after a 7-d running mean are shown in Fig. 10. From mid-March, F_c decreased with ice thickening and was close to zero in the end of November when the ice surface temperature was around 0°C (Fig. 10a). F_l was stable around –20.0 W/m^2 until the end of September, after which it decreased and become

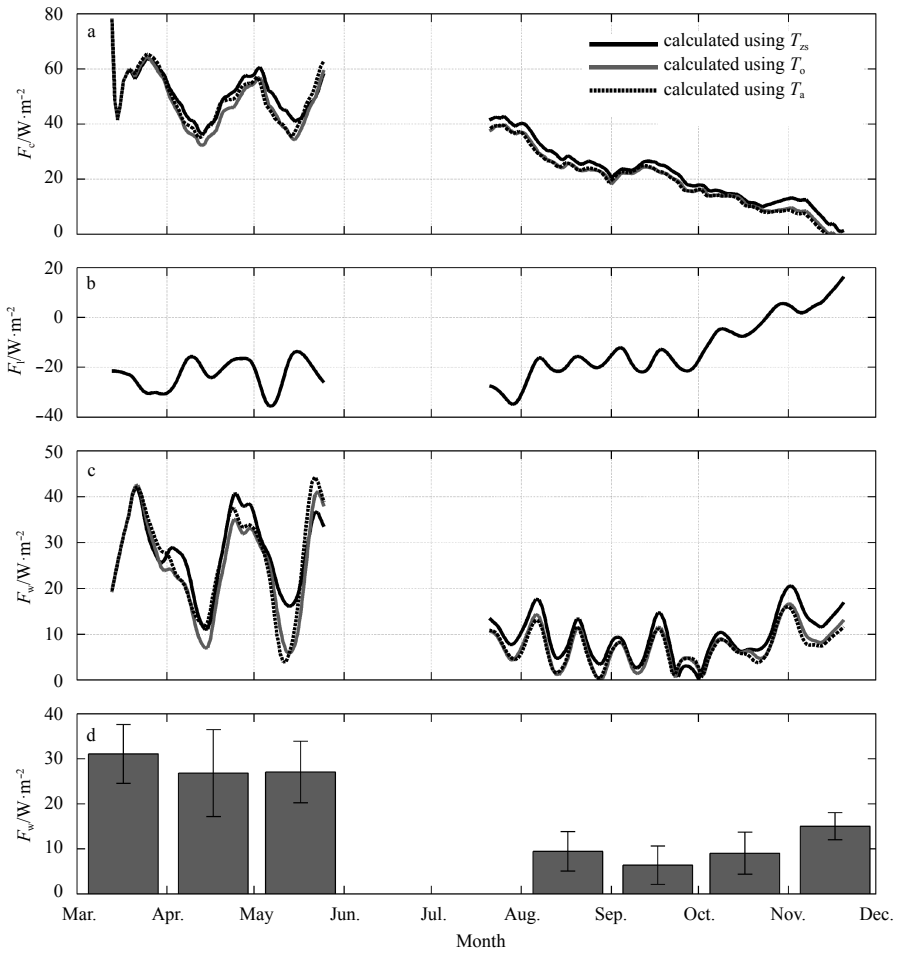

Fig. 10. Conductive heat flux at ice base (F_c) (a), latent heat flux (F_l) (b), ocean heat flux (F_w) (c), and monthly mean estimated ocean heat flux of FYI (d). All lines represent a 7-d moving average. Error bars in (d) represent the standard deviation of F_w in every month.

positive at the end of October. This indicated that the onset of the basal melting resulted in a reversed direction of the latent heat flux (Fig. 10b). F_w remained 20.0–40.0 W/m^2 during the initial ice growth period, with a maximum monthly mean value of (33.8 ± 7.5) W/m^2 in March. After July, F_w fell to around 10.0 W/m^2 (Fig. 10c). The minimum monthly mean was (4.7 ± 8.0) W/m^2 in September.

4 Discussion

Compared with the snow-free area, the thick snow cover on FYI usually slowed down the ice growth in winter, leading to thinner ice. However, for MYI in the Nella Fjord, thick snow cover prevented solar radiation from penetrating into ice in summer, so summer melting was limited to the snow layer (Maykut and Untersteiner, 1971; Yang et al., 2015a). Snow layer melting and re-freezing generated superimposed ice, then contributed to the total ice thickness. These mechanisms explain why the thick MYI was accompanied by deep snow cover. This phenomenon has been previously observed on MYI in McMurdo Sound (Gough et al., 2013).

Field records showed that the surface of SYI was almost level, and therefore the variation occurred in the bottom geometry. According to Archimedes' Principle, the scale of bottom topography variations can be ten times the scale of surface topographical variations when the horizontal scale exceeds the characteristic length of floating ice, which is tens of meters for 1 m ice. The largest spatial variations of SYI thickness was 33.0 cm, much smaller than MYI in the Arctic (~100 cm; Ackley et al., 1974), and SYI in McMurdo Sound (~ 50 cm; Gough et al., 2013).

In winter, the cold and arid climate may cause substantial sublimation. The sonar sensor recorded a total 1-cm surface sublimation in a no-snow-fall period from March 24 to April 3. The mean sublimation rate was 0.09 cm/d, in accordance with the estimation by Yang et al. (2015a). Sublimation became weaker when the surface became wet and ponds formed in the melting season.

The scaling and heat balance of FYI and MYI annual cycle was examined by a quasi-steady method (Leppäranta, 1993; Yang et al., 2015a). After the open water had refrozen in mid-February, FYI started to grow quickly because of the large temperature difference between ice surface and bottom, but SYI continued to melt until mid-April. The quasi-steady heat balance was the same as Eq. (1). It was clear that, since F_w>0, ice grows or melts depending on the thickness. If T_f–T_o≈10°C and F_w ≈30 W/m^2, we have the thickness for equilibrium status (no melting and growing), H ≈70 cm. This means ice will melt when thickness is more than 70 cm, which agrees with field observations. The bottom melting of SYI was also observed in McMurdo Sound (Gough et al., 2013), but the melting rate [(0.23 ± 0.02) cm/d] was much smaller than observed in this paper.

Estimating F_w of SYI in March using Eq. (1), the value was

around 100 W/m^2, which was much larger than the FYI range. In March, a soft layer was observed at 60.0–80.0 cm under the ice surface, which suggests that internal melting occurred. Modeling study by Zhao et al. (2017) showed that SYI in March had a nonlinear temperature profile and was isothermal in the low part. The uniform temperature structure prevented the conductive heat transport, leading to large internal and bottom melting.

5 Conclusions

The spatial and temporal evolution of the landfast ice, including FYI and SYI near the Antarctic ZS during December 2011 to December 2012 was studied using the field observations of the wintering team. The year-long measurements of SYI and winter surveys at several sections across the whole Nella Fjord were conducted for the first time.

The landfast ice in the Nella Fjord showed melt ponds from early December 2011, then ice cover partly broke in late January after a strong cyclone, and open water re-froze in the middle of February 2012 when the air temperature decreased. Other areas of ice surrounded by icebergs and small islands survived until the next winter. This allowed FYI and SYI to be simultaneously observed near ZS for the first time.

In March FYI grew quickly with a mean rate of 0.8 cm/d, but SYI experienced a rapid melting with a mean rate of 2.7 cm/d, which have been related to the nonlinear temperature profile and internal ice melting (Zhao et al., 2017). The SYI started to grow quickly from mid-April and reached the maximum thickness of 167.0 cm, a little larger than FYI maximum thickness of 160.5 cm. The FYI thickness showed minor spatial variations (~1.0 cm), but SYI thickness varied substantially with the largest variation 33.0 cm observed on March 23. This large thickness variation was associated with the particularly uneven SYI bottom.

Snow distribution largely depended on the surface roughness. According to sonar records, large snowfall events rarely occurred before June, which was concordant with observations at the Progress Station. Most snowfall was promptly blown away by the strong wind. The largest snow thickness detected by sonar was 31.0 cm at the end of October. Records at P1, P2, and the tripod did not support the maximum value recorded by sonar, suggesting that manual observations may miss important information because of their low frequency.

Sectional surveys in the Nella Fjord were carried out in winter and the results showed that snow and ice showed a similar pattern of "east thicker, west thinner". The spatial mean snow and ice thickness were 11.3 cm and 202.7 cm, respectively, which was much larger than FYI. The prevailing wind and topography influenced the spatial distribution of snow thickness and then snow melting in summer contributed substantially to MYI thickness as the form of superimposed ice. This mechanism explained the similar snow and ice pattern for MYI in the Nella Fjord.

The estimated oceanic heat flux had a similar annual cycle to that shown by Lei et al. (2010) at ZS and Heil et al. (1996) at Davis, but was different from the two-peak pattern at Mawson (Allison, 1981). The annual average oceanic heat flux of 15.6 W/m^2, was larger than 5.6 W/m^2 at ZS in 2006 (Lei et al., 2010), but similar to the findings of Yang et al. (2015a) who estimated the oceanic heat flux of the landfast ice off ZS with a 1-D sea ice thermodynamics model.

It should be noted that the lack of ice core data caused the insufficient analysis of SYI melting and superimposed ice contribution to MYI in this study. Ice temperature/salinity profiles and oceanographic observations beneath the ice should be carried out simultaneously in future to further increase our understanding of the mass balance of FYI and SYI near ZS.

Acknowledgments

The field observations were strongly supported by the Chinese Antarctic Zhongshan Station and the 2011/2012 wintering team, especially Li Yufeng. We would like to show our great appreciation.

References

Ackley S F, Hibler W D, Kugzruk F K, et al. 1974. Thickness and roughness variations of Arctic multi-year sea ice. Proceedings of Ocean 74-IEEE International Conference Engineering in the Ocean Environment. Halifax, Nova Scotia: 109–117

Allison I. 1981. Antarctic ice growth and oceanic heat flux. Proceedings of the Canberra Symposium, IAHS Publications, 131: 161–170

Fraser A D, Massom R A, Michael K J, et al. 2012. East Antarctic Fast Sea Ice Distribution and Variability, 2000-08. Journal of Climate, 25(4): 1137–1156, doi: 10.1175/JCLI-D-10-05032.1

Giles K A, Laxon S W, Ridout A L. 2008. Circumpolar thinning of Arctic sea ice following the 2007 record ice extent minimum. Geophysical Research Letter, 35: L22502, doi: 10.1029/2008GL035710

Gough A J, Mahoney A R, Langhorne P J, Haskell T G. 2013. Salinity evolution and mechanical properties of snow-loaded multiyear sea ice near an ice shelf. Antarctic Science, (25): 821–831

He J F, Chen B, Wu K. 1998. Developing and structural characteristics of first-year sea ice and with effects on ice algal biomass of zhongshan station, east Antarctica. Journal of Glaciology and Geocryology, 4: 358–367

Heil P, Allison I, and Lytle V I. 1996. Seasonal and interannual variations of the oceanic heat flux under a fast Antarctic ice cover. Journal of Geophysical Research, 101: 25,741–25,752, doi: 10.1029/96JC01921

Heil P. 2006. Atmospheric conditions and fast ice at Davis, East Antarctica: A case study. Journal of Geophysical Research, 111: C05009

Heil P, Gerland S, Granskog M A. 2011. An Antarctic monitoring initiative for fast ice and comparison with the Arctic. The Cryosphere Discussion, 5: 2437–2463, doi: 10.5194/tcd-5-2437-2011

Hoppmann M, Nicolau M. 2012. The influence of platelet ice and Snow on Antarctic Fast Sea Ice. From Knowledge to Action-IPY2012, Montréal, Canada

Kawamura T, Oshima K I, Takizawa T, et al. 1997. Physical, structural and isotopic characteristics and growth processes of fast sea ice in Lützow-Holm Bay, Antarctica. Journal of Geophysical Research, 102: 3345–3355, doi: 10.1029/96JC03206

Kwok R, Sulsky D. 2010. Arctic Ocean Sea ice thickness and kinematics: Satellite retrievals and modeling. Oceanography, 23(4): 134–143, doi: 10.5670/oceanog

Lei Ruibo, Li Zhijun, Cheng Bin, et al. 2010. Annual cycle of fast sea ice in Prydz Bay, east Antarctica. Journal of Geophysical Research, 115: C02006

Leppäranta M. 1993. A review of analytical models of sea-ice growth. Atmosphere-Ocean, 31(1): 123–138, doi: 10.1080/07055900.1993.9649465

Liu Jiping, Curry J A. 2010. Accelerated warming of the Southern Ocean and its impact on the hydrological cycle and sea ice. PNAS, 107(34): 14987–14992, doi: 10.1073/pnas.1003336107

Lu Peng, Li Zhijun. 2014. Uncertainties in retrieved ice thickness from freeboard measurements due to surface melting. Annals of Glaciology, 55(66)

Lytle V I, Massom R, Bindoff N, et al. 2000. Wintertime heat flux to the underside of east Antarctic pack ice. Journal of Geophysical Research, 105(28): 759–769

Maykut G A, Untersteiner N. 1971. Some results from a time dependent thermodynamic model of sea ice. Journal of Geophysical Research, 76: 2–4

McPhee M G, Untersteiner N. 1982. Using sea ice to measure vertical heat flux in the ocean. Journal of Geophysical Research, 87: 2071–2074, doi: 10.1029/JC087iC03p02071

Parkinson C L, Cavalieri D J. 2012. Antarctic sea ice variability and trends, 1979-2010. The Cryosphere, 6(2): 871–880

Perovich D K, Elder B. 2002. Estimates of ocean heat flux at SHEBA. Geophysical Research Letter, 29(9): 1344

Purdie C R, Langhorne P J, Leonard G H, et al. 2006. Growth of first-year fast Antarctic sea ice determined from winter temperature measurements. Annals of Glaciology, 44: 170–176, doi: 10.3189/172756406781811853

Tang Shulin, Qin Dahe, Ren Jiawen. 2006. Sea ice characteristics between Middle Weddell Sea and Prydz Bay, Antarctic during the 2003 Australian summer. Earth Science Frontiers, 13(3): 213–218

Tang Shulin, Qin Dahe, Ren Jiawen, et al. 2007. Structure, salinity and isotopic composition of multi-year fast sea ice in Nella Fjord, Antarctica. Cold Regions Science and Technology, 49: 170–177, doi: 10.1016/j.coldregions.2007.03.005

Worby A P, Geiger C A, Paget M J, et al. 2008. Thickness distribution of Antarctic sea ice. Journal of Geophysical Research, 113: C05S92

Yang Yu, Leppäranta M, Li Zhijun, et al. 2015a. Model simulations of the annual cycle of the fast ice thickness in the East Siberian Sea. Advances in Polar Sciences, 26(2): 168–178

Yang Yu, Li Zhijun, Leppäranta M, et al. 2015b. Modelling the thickness of fast sea ice in Prydz Bay, East Antarctica. Antarctic Science, 28(1): 59–70

Zhao Jiechen, Cheng Bin, Yang Qinghua, et al. 2017. Observations and modelling of first-year ice growth and simultaneous second-year ice ablation in the Prydz Bay, East Antarctica. Annals of Glaciology, 58: 59–67, doi: 10.1017/aog.2017.33